Modeling low order aberrations in laser guide star adaptive optics systems

KAON #477

Richard M. Clare and Marcos A. van Dam
W. M. Keck Observatory, 65-1120 Mamalahoa Highway, Kamuela HI 96743
rclare@keck.hawaii.edu

Antonin H. Bouchez
Caltech Optical Observatories, M/S 105-24, Pasadena, CA 91125

Abstract: When using a laser guide star (LGS) adaptive optics (AO) system, quasi-static aberrations are observed between the measured wavefronts from the LGS wavefront sensor (WFS) and the natural guide star (NGS) WFS. These LGS aberrations, which can be as much as 1200 nm RMS on the Keck II LGS AO system, arise due to the finite height and structure of the sodium layer. The LGS aberrations vary significantly between nights due to the difference in sodium structure. In this paper, we successfully model these LGS aberrations for the Keck II LGS AO system. We use this model to characterize the LGS aberrations as a function of pupil angle, elevation, sodium structure, uplink tip/tilt error, detector field of view, the number of detector pixels, and seeing. We also employ the model to estimate the LGS aberrations for the Palomar LGS AO system, the planned Keck I and the Thirty Meter Telescope (TMT) LGS AO systems. The LGS aberrations increase with increasing telescope diameter, but are reduced by central projection of the laser compared to side projection.

OCIS codes: (010.1080) Adaptive optics;(010.7350) Wave-front sensing.

References and links

1. J. W. Hardy, *Adaptive Optics for Astronomical Telescopes* (Oxford University Press, New York 1998).
2. C. E. Max, "Laser guide star operational issues," in *Laser Guide Star Adaptive Optics for Astronomy*, N. Ageorges and C. Dainty, eds. (Kluwer, Dordrecht, 1997), 89-106.
3. D. L. Fried and J. F. Belsher, "Analysis of fundamental limits to artificial-guide-star adaptive-optics-system performance for astronomical imaging," J. Opt. Soc. Am A **11**, 277-287 (1994).
4. M. A. van Dam, A. H. Bouchez, D. Le Mignant and P. L. Wizinowich "Quasi-static aberrations induced by laser guide stars in adaptive optics," Opt. Express **14**, 7535-7540 (2006).
5. P. L. Wizinowich, D. Le Mignant, A. H. Bouchez, R. D. Campbell, J. C. Y. Chin, A. R. Contos, M. A. van Dam, S. K. Hartman, E. M. Johansson, R. E. Lafon, H. Lewis, P. J. Stomski, D. M. Summers, C. G. Brown, P. M. Danforth and D. M. Pennington, "The W. M. Keck Observatory laser guide star adaptive optics system: overview," PASP **118**, 297-309 (2006).
6. M. A. van Dam, A. H. Bouchez, D. Le Mignant, R. D. Campbell, J. C. Y. Chin, S. K. Hartman, E. M. Johansson, R. Lafon, P. J. Stomski, Jr., D. M. Summers and P. L. Wizinowich, "The W. M. Keck Observatory laser guide star adaptive optics system: performance characterization," PASP **118**, 310-318 (2006).
7. D. Summers, A. H. Bouchez, J. Chin, A. Contos, S. Hartman, E. Johansson, R. Lafon, D. Le Mignant, P. Stomski, M. A. van Dam and P. L. Wizinowich, "Focus and pointing adjustments necessary for laser guide star adaptive optics at the W.M. Keck Observatory," in *Advancements in Adaptive Optics*, D. Bonaccini Calia, B. L. Ellerbroek and R. Ragazzoni, eds, Proc. SPIE **5490**, 1117-1128 (2004).
8. G. Herriot, P. Hickson, B. L. Ellerbroek, D. A. Andersen, T. Davidge, D. A. Erickson, I. P. Powell, R. M. Clare, L. Gilles, C. Boyer, M. Smith, L. Saddlemyer, J.-P. Vran, "NFIRAOS: TMT narrow field near-infrared facility adaptive optics," in *Advances in Adaptive Optics II*, B. L. Ellerbroek, D. Bonaccini Calia eds., Proc. SPIE **6272**, 62720Q (2006).

#79346 - $15.00 USD Received 24 Jan 2007; revised 19 Mar 2007; accepted 29 Mar 2007; published 3 Apr 2007

9. R. M. Clare, B. L. Ellerbroek, G. Herriot, and J. P. Véran, "Adaptive optics sky coverage modeling for extremely large telescopes," Appl. Opt. **45**, 8964-8978 (2006).
10. P. L. Wizinowich , J. Chin, E. Johansson, S. Kellner, R. Lafon, D. Le Mignant, C. Neyman, P. Stomski, D. Summers, R. Sumner, M. van Dam,"Adaptive Optics Developements at Keck Observatory," in *Advances in Adaptive Optics II*, B. L. Ellerbroek, D. Bonaccini Calia eds., Proc. SPIE **6272**, 627209 (2006).
11. R. Dekany, V. Velur, H. Petrie, A. Bouchez, M. Britton, A. Morrissett, R. Thicksten, M. Troy, C. Shelton, T. Troung, J. Roberts, G. Brack, T. Trinh, S. Bikkannavar, S. Guiwits, J. Angione, F. Shi, E. Kibblewhite "Laser Guide Star Adaptive Optics on the 5.1 Meter Telescope at Palomar Observatory," AMOS Technical Conference Proceedings (2005).
12. R. J. Noll, "Zernike polynomials and atmospheric turbulence," J. Opt. Soc. Am. **66**, 207-211 (1976).
13. P. S. Argall, O. N. Vassiliev, R. J. Sica, M. M. Mwangi,"Lidar Measurements Taken With a Large-Aperture Liquid Mirror. 2. Sodium Resonance-Fluorescence System," Appl. Opt., **39**, 2393-2400 (2000).
14. A. Tokovinin and T. Travouillon, "Model of optical turbulence profile at Cerro Pachón," Mon. Not. R. Astron. Soc. **365** 1235-1242 (2006).
15. L. A. Poyneer, "Scene-based Shack-Hartmann wave-front sensing: analysis and simulation," Appl. Opt. **42**, 5807-5815 (2003).
16. L. Gilles and B. L. Ellerbroek, "Shack-Hartmann wavefront sensing with elongated sodium laser beacons: centroiding versus matched filtering," Appl. Opt. **45**, 6568-6576 (2006).
17. J. Nelson, G. H. Sanders, "TMT status report,"in *Ground-based and Airborne Telescopes*, L. M. Stepp ed., Proc. SPIE **6267**, 745-761 (2006).
18. J. W. Beletic, "Follow the yellow-orange rabbit: a CCD optimized for wavefront sensing a pulsed sodium laser guide star," in *Optical and Infrared Detectors for Astronomy* J. D. Garnett, J. W. Beletic; eds., Proc. SPIE **5499**, 302-309 (2004)

1. Introduction

The resolution of images of astronomical objects captured by ground-based telescopes is limited by the time-varying wavefront aberrations induced by the earth's atmosphere and by imperfections in the telescope optics. These aberrations can be corrected in real time using adaptive optics (AO) [1]. The sky coverage of natural guide star (NGS) AO systems is limited by the need for a bright reference star for wavefront sensing close to the science object. In order to overcome this problem, sodium laser guide star (LGS) AO systems [2] create an artificial reference beacon in the mesospheric sodium layer in the science direction for sensing the wavefront aberrations.

There are, however, a number of fundamental differences between the wavefront measured with a LGS and the actual aberrations to which starlight is subjected. Firstly, because the LGS is located at a finite height (of approximately 90 km) and not at infinity, the LGS sees a cone of turbulence rather than a cylinder. This is referred to as the cone effect [3]. Secondly, the altitude of the sodium layer is constantly changing, which the LGS wavefront sensor (WFS) sees as a change of focus. This is compensated by changing the LGS WFS focus position. The remaining differences are the so-called LGS aberrations [4], and arise due to the finite height and non-zero thickness of the sodium layer.

In Ref. [4], we presented the LGS aberrations that have been measured on the Keck II LGS AO system and described the reasons why they arise. An initial attempt to model the LGS aberrations was also made. Here in this paper, we create a more detailed simulation model to calculate the LGS aberrations in order to characterize the LGS aberrations in terms of the pertinent parameters. We also use this simulation model to estimate the LGS aberrations for existing and planned LGS systems.

The Keck II LGS AO system has a 589 nm wavelength laser which is projected using a 50cm launch telescope on the side of the telescope, 6.2 m from the optical axis of the telescope [5, 6]. The LGS WFS is a Shack-Hartmann WFS. For a Shack-Hartmann sensor with a LGS at a finite height and non-zero thickness, the spot at each subaperture is elongated due to the parallax effect. The elongation of the Shack-Hartmann spots, η, for the LGS WFS is approximately

#79346 - $15.00 USD Received 24 Jan 2007; revised 19 Mar 2007; accepted 29 Mar 2007; published 3 Apr 2007

given by [4]

$$\eta = \frac{\cos(\zeta) bt}{h^2}, \tag{1}$$

where ζ is the zenith angle, b is the baseline distance between the launch telescope and the subaperture, t is the thickness of the sodium layer, and h is the height of the sodium layer above the telescope.

The probable sources of the LGS aberrations are identified in Ref. [4], and are summarized here:

- Asymmetric spot elongation: the LGS spots are asymmetric because the elongation is inversely proportional to height squared (see Eq. (1)), so the bottom of the profile appears more elongated than the top of the profile.
- Quad-cell centroiding: for an asymmetric LGS spot, the quad-cell centroid is not equal to the center-of-mass of the LGS spot.
- Truncation of the LGS spots: a bias is introduced to the centroid measurement if the LGS spot is asymmetric and truncated by a field stop or pixel boundaries.
- Telescope and AO system aberrations: because the laser guide star is situated at 90km and the NGS at infinity, the LGS may be subjected to different aberrations while passing through the AO optical relay.

The LGS aberrations, and also the focus variations due to changes in the altitude of the sodium layer, are measured on the Keck II LGS AO system with the low bandwidth wavefront sensor (LBWFS), which guides on the TT NGS. 20 % of the light from the TT NGS is passed to the LBWFS, which is a 20×20 Shack-Hartmann WFS, the same order as the LGS WFS. The focus aberration measured by the LBWFS is used to update the LGS WFS focus position [7], and the higher order aberrations are used to update the reference centroids for the LGS WFS [6]. If the NGS is sufficiently bright ($m_V \leq 18$), the LGS aberrations can be measured with the LBWFS and corrected. If the NGS is fainter than this, or if the telescope pupil is rotating quickly, the LGS aberrations cannot be adequately compensated with the LBWFS alone. If one could predict the quasi-static LGS aberrations without measuring them, one could use fainter TT NGS, increasing the sky fraction available for AO-compensated observing.

With the LGS aberrations corrected using the LBWFS, the total RMS error of the Keck II LGS system when using a R=10 magnitude NGS is 357 nm [6]. As will be discussed in Section 2, the LGS aberrations as measured on the Keck II LGS system can be of the order of 1200 nm RMS. The delivered wavefront error would therefore be dominated by LGS aberrations if not correctly predicted or accurately measured.

A number of new LGS AO systems for existing and future telescopes are in the design stages, such as the TMT AO system, NFIRAOS, [8, 9] and the Keck I LGS AO system [10]. Because the LGS aberrations measured with the Keck II system are so significant, it is important to understand and be able to model the LGS aberrations before building the next generation of LGS AO systems. In this paper, we model the LGS aberrations observed with the Keck II LGS AO system, and apply this model to current designs for TMT and Keck I LGS AO, and to the existing Palomar LGS AO system [11].

The format for the rest of this paper is as follows: we discuss the LGS aberrations measured on the Keck II LGS AO system in Section 2. We derive our model for the LGS aberrations and compare with the observed LGS aberrations on Keck II in Section 3. In Section 4, we investigate the parameter space that affects the LGS aberrations. In Section 5, we estimate the LGS aberrations for planned future AO systems. Finally, in Section 6, we draw our conclusions on the LGS aberrations.

#79346 - $15.00 USD Received 24 Jan 2007; revised 19 Mar 2007; accepted 29 Mar 2007; published 3 Apr 2007

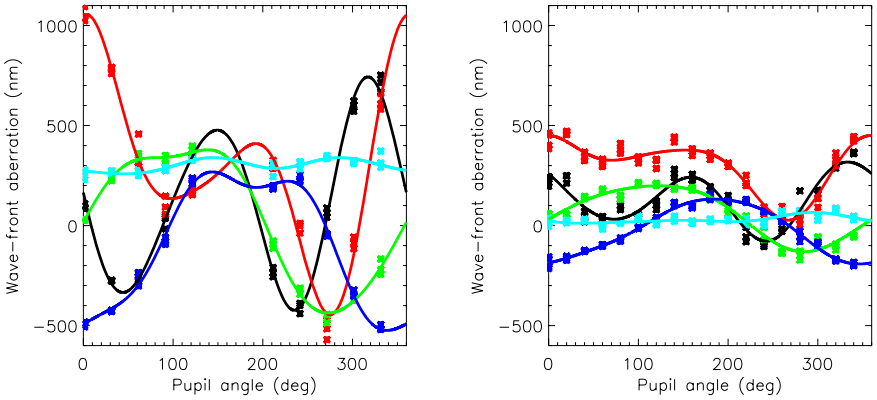

Fig. 1. The measured LGS aberrations as a function of pupil angle near zenith for the night of (a) 26 January 2005, and (b) 20 July 2006. The curves are, 0° astigmatism (red), 45° astigmatism (black), *y*-coma (green), *x*-coma (dark blue) and spherical aberration (light blue).

2. Measuring the LGS aberrations

The LGS aberrations were measured on the telescope by locking the TT loop on a bright NGS, and by locking the deformable mirror (DM) loop on the LGS and setting the LGS reference centroids to be all zeros. The pupil was kept fixed on both the LGS WFS and LBWFS. The pupil angle was rotated and LBWFS images taken at regular intervals. The pupil angle thus specifies the position of the laser relative to the WFS subapertures. The laser is located at the top of the LGS WFS and LBWFS images for Keck II when the pupil angle is 116.6°. We will define a pupil angle of 0° to be at the top of the pupil in this paper in order to be consistent between telescopes. Thus the pupil angles reported here for Keck II lag the true pupil angle by 116.6°. Consequently, Fig. 1(a) of this paper lags Fig. 2 of [4] by 116.6°.

The LGS aberrations are calculated as a least-squares fit to the low order Zernike polynomials from the displacements (centroids) of each subaperture of the LBWFS. We choose to use Zernike polynomials to model the aberrations because the low order polynomials represent the well known optical aberrations of astigmatism, coma etc. The first 11 Zernike polynomials as ordered by Noll [12] (i.e. up to spherical aberration, but ignoring tip, tilt and focus, which are independently corrected, and piston) contain 89% of the mean-squared LGS aberrations. That is, 89% of the mean-squared aberrations as seen on the LBWFS can be fitted with these seven Zernike polynomials. The low order LGS aberrations, ϕ, are therefore given by

$$\phi = \sum_{i=5}^{11} a_i Z_i \tag{2}$$

where Z_i is the i^{th} Zernike polynomial with coefficient a_i.

We display the measured LGS aberrations versus pupil angle for the astigmatism, coma, and spherical aberration for the nights of 26 January 2005 and 20 July 2006 in Fig. 1. These observations were made near zenith. A best-fit spline is superimposed for each mode. We see from these graphs that there are significant astigmatism, coma and spherical aberrations and that these aberrations vary with pupil angle. The astigmatism modes both exhibit sinusoidal

#79346 - $15.00 USD Received 24 Jan 2007; revised 19 Mar 2007; accepted 29 Mar 2007; published 3 Apr 2007

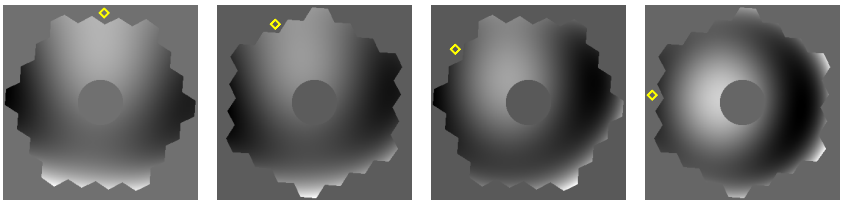

(a) (b) (c) (d)

Fig. 2. The total low order LGS aberrations for the night of 26 January 2005 at a pupil angle of (a) 0°, (b) 30°, (c) 60°, and (d) 90°. The yellow diamond indicates the approximate position of the laser.

behavior with π periodicity with respect to pupil angle. The astigmatism modes are non-zero mean on both nights. The peaks and valleys of both astigmatism modes are different on the two cycles. This is consistent between the two nights. The coma modes also exhibit sinusoidal behavior with respect to pupil angle, with 2π periodicity. The astigmatism modes are π rotationally symmetric and the coma modes 2π rotationally symmetric, which explains the periodicity of these aberrations as the laser position is rotated about the lenslet array. Both the coma modes are non-zero mean on both nights. The spherical aberration is non-zero mean on both nights. Any dependence of the spherical aberration on the pupil angle is not clear from these nights.

There is significant variation in the magnitudes of LGS aberrations between nights, as shown in Fig. 1, although the phase of the astigmatism and coma modes is consistent between nights. The spherical aberration is particularly inconsistent between nights, with the mean differing by approximately a factor of seven.

The total low order LGS aberration is shown in Fig. 2 for pupil angles of 0°, 30°, 60°, and 90° for the night of 26 January 2005. Fig. 2 shows that the LGS aberrations do largely rotate with the laser, but not exactly.

3. Modeling theory

In this section, we present our method for modeling the LGS aberrations, and compare the modeled aberrations using this method with the measured aberrations presented in Section 2. The first step in calculating the LGS aberrations is to calculate the LGS WFS subaperture images. We do this using geometric optics, i.e. ray-tracing. In this model, the LGS images are a function of the launch telescope position, subaperture geometry, zenith angle (ζ), atmospheric seeing (ε), size and number of detector pixels, and the sodium profile ($n(z)$) where z is altitude.

We model the laser as a cylindrical beam of 0.5 m. The geometric image of the i^{th} LGS WFS image, $g(i;x,y)$, is the integral of the sodium profile $n(z)$ that is illuminated by the laser beam and intersects the ray traced by each WFS detector pixel

$$g(i;x,y) = \int_{z_0(i;x,y)}^{z_1(i;x,y)} \frac{n(z)}{\cos(\theta(i;x,y))\cos(\zeta)} dz, \tag{3}$$

where $\theta(i;x,y)$ is the angle between the center of each pixel of the ith subaperture and the laser beam. The limits of the integral denote the range of altitudes of the sodium layer that each WFS detector pixel sees, as shown in Fig. 3.

The i^{th} LGS WFS image, $p(i;x,y)$, is the convolution of the ith geometric image, $g(i;x,y)$, with the seeing function $s(x,y)$ and the charge diffusion function $m(x,y)$, which accounts for the effective widening of the pixels by charge diffusion within the CCD,

$$p(i;x,y) = g(i;x,y) \odot s(x,y) \odot m(x,y). \tag{4}$$

#79346 - $15.00 USD Received 24 Jan 2007; revised 19 Mar 2007; accepted 29 Mar 2007; published 3 Apr 2007

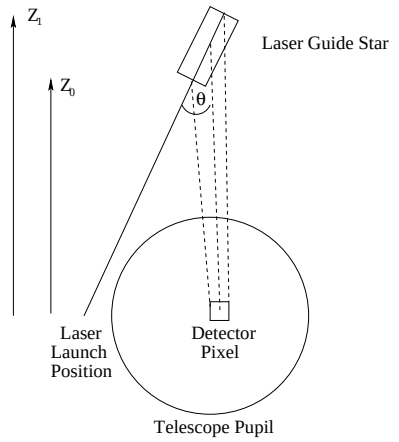

Fig. 3. The geometrical model of the pupil, laser, detector pixel and laser guide star.

The seeing function $s(x,y)$ is a Gaussian function of FWHM equal to the quadrature sum of two times the atmospheric seeing, ε, (up and down). Similarly, the charge diffusion function $m(x,y)$ of the detector pixels is a Gaussian function, with the FWHM assumed to be half the plate scale of the detector pixels.

We find the (quad-cell) centroids, $(c_x(i),c_y(i))$, of the LGS WFS images with the center-of-mass centroid

$$c_x(i) = \frac{\Sigma x p(i;x,y)}{\Sigma p(i;x,y)} \tag{5}$$

$$c_y(i) = \frac{\Sigma y p(i;x,y)}{\Sigma p(i;x,y)} \tag{6}$$

The laser spot moves on the sky, which is due to tilt introduced in the upward path through atmospheric turbulence, telescope vibrations, and wind-shake [5]. The position of the laser on the sky is stabilized with a TT mirror in the laser launch telescope. This is referred to as uplink TT (UTT) correction. The UTT of the laser telescope is modeled by shifting the LGS WFS images such that the mean centroid in x and y is zero,

$$\Sigma c_x = \Sigma c_y = 0. \tag{7}$$

From the centered LGS WFS images, the displacement of the ith subaperture, $d(i) = (d_x(i),d_y(i))$, is calculated by using the Fourier shift theorem to shift the LGS images

$$p'(i;x,y) = \mathscr{F}^{-1}\left(\mathscr{F}\left(p(i;x,y)\right)\exp[j2\pi(d_x(i)x+d_y(i)y)]\right) \tag{8}$$

such that the centroids of the ith shifted image are zero, i.e. $(c'_x(i),c'_y(i)) = 0$, where the prime notation indicates the shifted image.

The LGS aberrations in terms of Zernike coefficients, a, are calculated from the displacements, d, by a least-squares reconstructor to the low order Zernike polynomials

$$a = (H^T H)^{-1} H^T d, \tag{9}$$

where H is the interaction matrix relating the slopes to Zernike polynomials.

A representative sodium profile, $n(z)$, that we use to model the Keck II system is shown in Fig. 4(a). This profile was generated as a best fit of the sum of two Gaussians, of σ 3.5 km

#79346 - $15.00 USD Received 24 Jan 2007; revised 19 Mar 2007; accepted 29 Mar 2007; published 3 Apr 2007

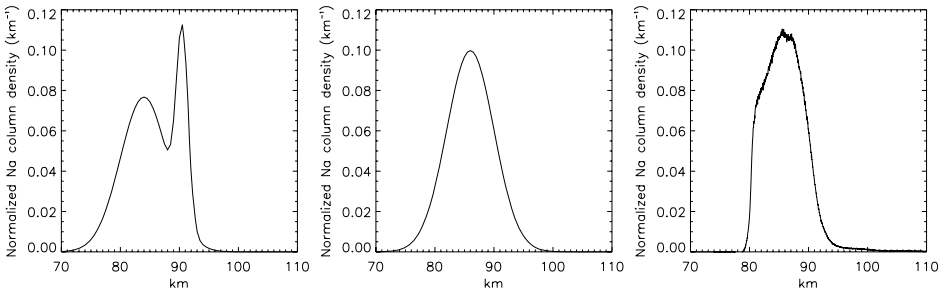

(a) (b) (c)

Fig. 4. The normalized sodium profiles: (a) best-fit sum of 2 Gaussians for the night of January 26 2005, (b) best-fit single Gaussian for the night of January 26 2005, and (c) median profile from the University of Western Ontario LIDAR.

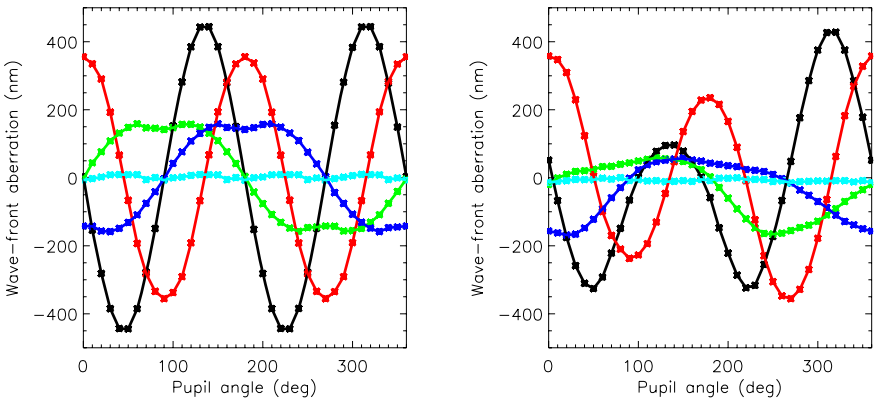

(a) (b)

Fig. 5. The modeled LGS aberrations as a function of pupil angle at zenith for using the sum of two Gaussians sodium profile assuming (a) no UTT error, and (b) a UTT error of (0.1″, -0.1″). The curves are 0° astigmatism (red), 45° astigmatism (black), *y*-coma (green), *x*-coma (dark blue) and spherical aberration (light blue).

and 1.0 km at heights of 84.0 km and 94.5 km, to an acquisition camera image of January 26 2005, which was the night that the LGS aberrations of Fig. 1(a) were measured [4]. We also use a typical atmospheric seeing value of 0.5″ (0.5 arc sec). For now, we assume the LGS images are correctly centered on the quad-cells, i.e. there is no UTT error. Although there are 304 subapertures, the Keck system only uses the 240 subapertures that are illuminated by the rotating hexagonal pupil (active subapertures), and we include this in the model also. The detector for each subaperture is a quad-cell, with each pixel 2.1″ square. There is a circular field stop of radius 2.4″ located at the focus of the telescope.

The modeled LGS aberrations displayed in Fig. 5(a) exhibit many of the characteristics of the measured LGS aberrations in Fig. 1. For both the measured and modeled aberrations, both the astigmatism versus pupil angle curves are approximately sinusoidal and have π periodicity with respect to pupil angle. The modeled and measured astigmatism curves are in phase with each other. The magnitudes of the measured and modeled aberrations agree reasonably, given

#79346 - $15.00 USD Received 24 Jan 2007; revised 19 Mar 2007; accepted 29 Mar 2007; published 3 Apr 2007

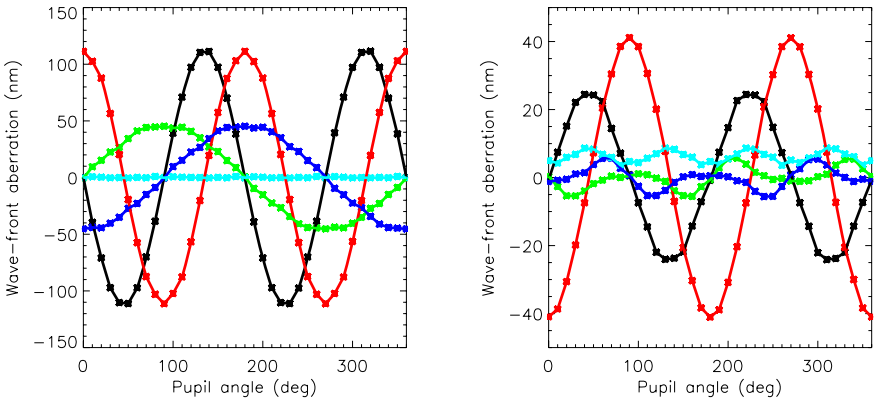

(a) (b)

Fig. 6. The modeled LGS aberrations as a function of pupil angle at zenith for (a) the Gaussian sodium profile and (b) the median LIDAR profile. The curves are, 0° astigmatism (red), 45° astigmatism (black), *y*-coma (green) and *x*-coma (dark blue) and spherical aberration (light blue).

the imprecise knowledge of the sodium profile and the sodium profile's importance on the magnitude of the LGS aberrations (see Section 4.1). The modeled astigmatism curves are zero-mean and the magnitudes of the peaks and troughs are equal in both cycles, unlike the measured aberrations. This is thought to be due to a de-centered field stop, and is investigated in Section 4.4.

The modeled and measured coma versus pupil angle curves are both approximately sinusoidal, with 2π periodicity with respect to pupil angle. The modeled and measured coma curves are in phase. Unlike the modeled coma curves, the measured coma curves are both non-zero mean, but this can be explained by a UTT error as explained in Section 4.4.

The modeled and measured spherical aberration curves do not agree in either magnitude or phase. The modeled spherical aberration is non-zero mean, and is $\pi/2$ periodic with respect to pupil angle. As will be discussed in Section 4.4, the non-zero mean nature of the measured spherical aberrations cannot be explained by an UTT error. The difference between the measured and modeled spherical LGS aberration could be due to telescope and AO system aberrations which are not modeled here.

4. Characterization of LGS aberrations

In this section, we use our model to characterize the LGS aberrations with respect to the parameter space for the Keck II LGS AO system. Unless otherwise stated, the parameter values used in this section are the same as those in Section 3.

4.1. Sodium structure

The magnitude of the LGS aberrations is strongly dependent on the structure of the sodium layer. The sodium structure can affect the bias due to truncation, and the bias due to using a quad-cell is affected by the asymmetry of the sodium structure. In order to demonstrate and quantify this dependence, we have simulated the Keck II system with the same parameters as Section 3, but using a sodium profile that is a Gaussian with σ of 4.0 km, located at an altitude of 86.0 km above the telescope, as shown in Fig. 4(b). The LGS aberrations for the single

#79346 - $15.00 USD Received 24 Jan 2007; revised 19 Mar 2007; accepted 29 Mar 2007; published 3 Apr 2007

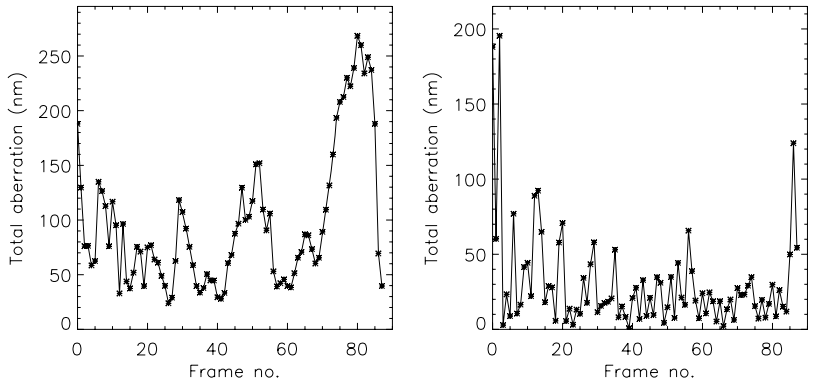

Fig. 7. (a) The modeled total magnitude of the LGS low order aberrations (nm) for Keck II versus frame number of the LIDAR profile. The frames are sampled 72 seconds apart. (b) The difference in the LGS aberrations (nm) between consecutive frames.

Gaussian sodium profile, which are plotted in Fig. 6(a), are at least four times smaller than for the aberrations for the sum of two Gaussians sodium profile, plotted in Fig. 5(a). This indicates that the LGS aberrations increase as a function of the asymmetry of the sodium profile.

We also simulate the Keck II system with the median profile as measured by the University of Western Ontario LIDAR in London, Canada [13]. This profile is shown in Fig. 4(c), and has a vertical resolution of 24 m. The LGS aberrations for this measured profile are significantly smaller than the measured LGS aberrations and the modeled LGS aberrations with either the Gaussian or sum of two Gaussians profiles. This is because the measured profile is narrower than either of the Gaussian profiles, and thus there is less truncation of the LGS spots, which is a significant source of the LGS aberrations. It is also interesting to note that while the astigmatism curves are still π periodic, the sign of the astigmatism coefficients is reversed for this median profile compared to the measured LGS aberrations and the modeled aberrations for both the Gaussian profiles. This is because the structure of this sodium layer induces a bias in the centroid measurement in the opposite direction to that of the Gaussian profiles, and consequently the sign of the LGS aberrations is reversed.

4.2. Temporal variation

On any night, the structure of the sodium layer is evolving. In order to investigate the temporal nature of the LGS aberrations, we use a time series of 88 sodium profiles measured using the University of Western Ontario LIDAR [13]. These profiles have a temporal resolution of 72 seconds and a spatial resolution of 24 m. The total modeled LGS aberrations for the Keck II LGS AO system for a pupil angle of 0° for these 88 sodium profiles are plotted in Fig. 7(a). The median total LGS aberration from this series of profiles is 76 nm, which is significantly less than observed on the telescope. The difference in the LGS aberrations in the low order modes between consecutive time stamps is shown in Fig. 7(b). The median difference in the LGS aberrations between consecutive frames is 20 nm.

#79346 - $15.00 USD Received 24 Jan 2007; revised 19 Mar 2007; accepted 29 Mar 2007; published 3 Apr 2007

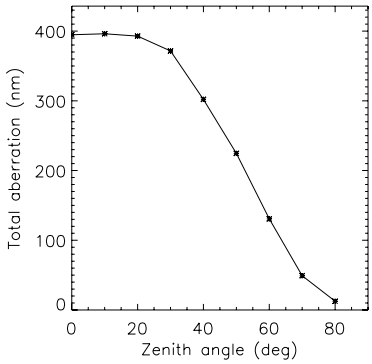

Fig. 8. The total simulated LGS aberration as a function of zenith angle (deg) for the Keck II system at 0° pupil angle.

4.3. Zenith angle

As shown in Eq. (1), the elongation of the LGS spot is proportional to the cosine of the zenith angle. The atmospheric seeing, ε, also increases with zenith angle by [1, 14]

$$\varepsilon(\zeta) = \varepsilon(0)\sec(\zeta)^{3/5}, \tag{10}$$

although as shown in Section 4.7, the dependence of the LGS aberrations on the seeing is negligible. In Fig. 8, the simulated total low order LGS aberration is plotted versus the zenith angle for a 0° pupil angle. The total aberration exhibits an approximately cosine dependence on the zenith angle, which is consistent with the elongation of the LGS WFS images being proportional to the cosine of the zenith angle.

4.4. Uplink tip-tilt (UTT) error

An UTT error of the laser beam leads to the LGS subaperture images being de-centered with respect to the subaperture optical axis. The effect of the UTT error is to produce a bias in the centroid measurement in the direction of the UTT error. If this bias is in the direction of the laser launch telescope, the bias adds to the existing biases due to truncation, asymmetric elongation and quad-cell centroiding, causing a larger peak/valley in the astigmatism curves. If, however, the UTT error is in the opposite direction of the laser launch telescope, the bias subtracts from the existing biases and consequently the magnitude of the peak/valley of the astigmatism curve is reduced. A similar error to UTT is caused by a de-centered field stop, which truncates the spots and creates a bias in the centroid in the direction of the de-centering. We believe that the pupil stop for the Keck II system could be de-centered, but we cannot verify this since we are unable to put a calibration laser at the correct focus of the LGS.

The modeled LGS aberrations for the Keck II system, with a UTT error of $0.1''$ in x and $-0.1''$ in y, are plotted in Fig. 5(b). This combination of UTT x and y error approximately gives the observed behavior of the astigmatism coefficients on both nights shown in Fig. 1. This combination of UTT x and y error also causes both coma curves to be non-zero mean, which is the observed behavior on both nights plotted in Fig. 1.

4.5. Wavefront sensor sampling

The number of detector pixels used to sample the LGS images also affects the LGS aberrations. With a standard center-of-mass centroid operator, the more pixels there are, the higher the

#79346 - $15.00 USD Received 24 Jan 2007; revised 19 Mar 2007; accepted 29 Mar 2007; published 3 Apr 2007

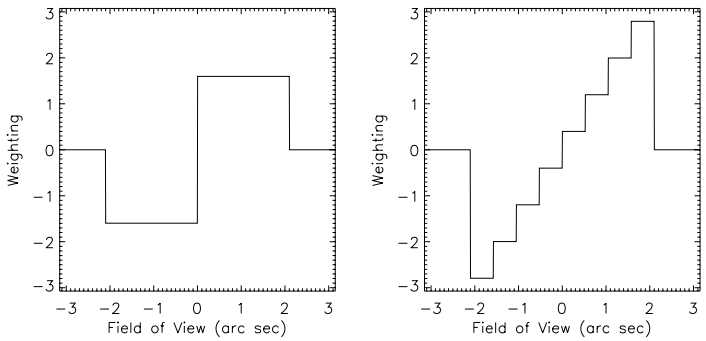

(a) (b)

Fig. 9. The weighting over the FOV for a 3.0″ spot with a center-of-mass centroid for (a) a quad-cell, and (b) 8×8 pixels.

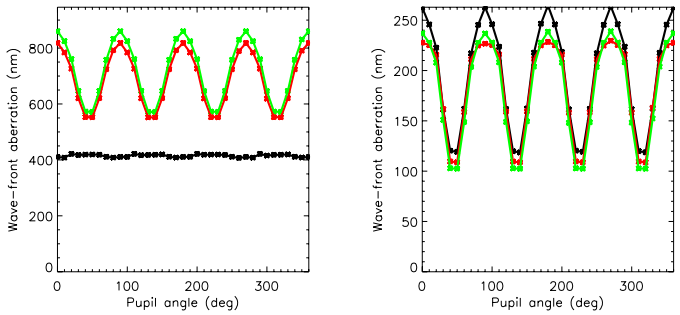

(a) (b)

Fig. 10. The total low-order LGS aberration for 2×2 (black), 4×4 (red) and 8×8 (green) pixels for (a) a FOV of 4.2″ and (b) a FOV of 8.4″.

weighting on the portion of the spot farthest away from the center. This is shown in Fig. 9 for a quad-cell and 8×8 pixels with a spot of dimension 3.0″ and total field of view (FOV) of 4.2″.

When an asymmetric spot is truncated, the part of the spot that is truncated, and hence given a weighting of zero, would otherwise have the highest weighting on the centroid. To see this effect, we subdivide the LGS spots in a quad-cell (i.e. 2×2 pixels), with 4×4 pixels and 8×8 pixels, keeping the total FOV constant. The field stop is square and equal to the FOV. We consider two cases: 1) where there is some truncation of the spots using a 4.2″ FOV, and 2) where there is no significant truncation of the spots using a 8.4″ FOV.

For the first case with a detector FOV of 4.2″ the total low-order LGS aberration is shown in Fig. 10(a). The LGS aberrations are smallest for 2×2 pixels, followed by 4×4 pixels and then 8×8 pixels. This is true for all pupil angles. The difference in going from a quad-cell to more pixels is greatest at 0°, 90°, 180° and 270° because this is when the truncation is greatest, so the amplification of the truncation by the centroid operator is also the greatest.

For the second case, where we use a much larger FOV (8.4″) to avoid any significant truncation of the LGS spots, the total LGS aberrations are plotted in Fig. 10(b). The total LGS aberration is largest for 2×2 pixels, with 4×4 and 8×8 pixels giving aberrations of approximately the same magnitude.

#79346 - $15.00 USD Received 24 Jan 2007; revised 19 Mar 2007; accepted 29 Mar 2007; published 3 Apr 2007

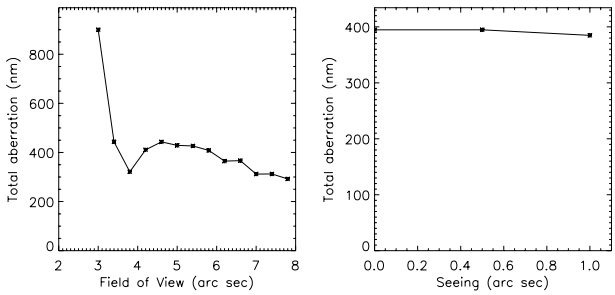

(a) (b)

Fig. 11. The total simulated LGS aberration for the Keck II system at 0° pupil angle and at zenith as a function of (a) the FOV, and (b) the atmospheric seeing.

To summarize the simulation results presented in this subsection on the number of pixels used to subdivide the LGS spots, we see that if there is significant truncation of the spots, the aberrations are reduced by using a quad-cell. This is because the centroid operator weights the truncated portion of the spot more with more pixels, and so the bias due to truncation is increased with more pixels. In contrast, if there is no significant truncation of the spots, the LGS aberrations are reduced with more pixels, because the bias due to using a quad-cell centroid is eliminated.

4.6. Detector field of view

The FOV of the LGS WFS affects the truncation of the LGS spots and hence the LGS aberrations. For the Keck II system, the FOV is equal to twice the plate scale of the quad-cell pixels. The total low order aberration as a function of the FOV for Keck II is shown in Fig. 11(a) at zenith for a pupil angle of 0°. For a small FOV (i.e. 3.0″), there is significant truncation of the LGS spots and the LGS aberrations are large. As the FOV increases, the truncation is reduced and the LGS aberrations decrease. There is a local minimum at approximately 3.8″ where there is some truncation of the LGS spots, but the bias due to this truncation cancels to some extent the bias due to the quad-cell centroid of the asymmetric spots. As we increase the FOV further, although the truncation of the spots is decreasing, the LGS aberrations increase. At a FOV of 8.0″ there is no significant truncation of the LGS spots and the LGS aberrations are at a minimum.

4.7. Atmospheric seeing

The LGS aberrations are weakly dependent on the atmospheric seeing. As shown in Eq. (4), the LGS images are convolved by the quadrature sum of the seeing (both up and down) and the charge diffusion of the pixels. In most cases, the charge diffusion (half the pixel scale) is significantly larger than twice the seeing, and so is the dominant term. Increasing the seeing can increase the truncation of the LGS images, increasing the bias due to truncation, but can also blur out the structure of the sodium layer, reducing another of the bias terms. As shown in Fig. 11(b), there is little dependence of the LGS WFS aberrations on the seeing over the expected range of seeing.

4.8. Centroiding algorithms

We compare using the correlation track algorithm [15] for determining the displacements of the LGS images with the center-of-mass centroid algorithm used previously. The correlation track

#79346 - $15.00 USD Received 24 Jan 2007; revised 19 Mar 2007; accepted 29 Mar 2007; published 3 Apr 2007

algorithm works by correlating the LGS image with a reference image for that subaperture. We have chosen to use the LGS images as the reference images, but with each reference image shifted such that the center-of-mass of the reference image is zero. The displacement of each subaperture is then found by shifting each subaperture image from its zero mean position to where the centroid from the correlation algorithm is zero.

Simulations using the correlation track and center-of-mass centroiding yielded LGS aberrations of exactly the same magnitude. The reason for this is that we are driving the centroid to zero, and the centroid will be zero when the LGS image is equal to the reference image. But the reference image has zero center-of-mass centroid, so the correlation track algorithm will give the same centroid as the center-of-mass centroid. The same result will be true for the matched filter algorithm [16] for finding the subaperture displacements, because the reference images will still be truncated, and the true center unknown.

The correlation track method does improve the linearity of the wavefront sensor response, and consequently it is possible to drive the correlation centroid to zero more quickly than the center-of-mass centroid.

5. Other LGS AO systems

In this section, we apply the model for the LGS aberrations derived in Section 3 to the Palomar LGS AO system, and the planned Keck I and TMT LGS AO systems. In particular, we are interested in determining how the aberrations vary with telescope diameter for a centrally projected laser.

5.1. Palomar

The 5.1 m Hale telescope at Mt. Palomar has a centrally projected laser [11]. The LGS WFS is a Shack-Hartmann with 16×16 subapertures. Each subaperture has a quad-cell detector with pixels of dimension $1.2''$ for a FOV of $2.4''$. There are 241 active subapertures. Using our model, we calculate the total low order LGS aberration expected for Palomar to be 5 nm. The only non-zero coefficient of the first 30 Zernike polynomials is spherical aberration which is 5 nm. For Palomar, the LGS aberrations are insignificant, due to the central projection of the laser and the small aperture size.

5.2. Keck I LGS AO

Keck I will project the laser from behind the center of the secondary mirror. We consider the CCID-56 detector, which has 8×8 pixels with a projected size of $0.6''$ as the WFS CCD. There is a square field stop of $4.8''$ a side. Because the laser is projected from behind the secondary, there is no dependence of the aberrations on pupil angle, and instead we tabulate the LGS aberrations in Table 1. Most of the low order Zernike coefficients are negligible, so we only tabulate any of the Zernike polynomials with significant power. The phase screen represented by the sum of the low order aberrations for Keck I is displayed in Fig. 12.

Figure 12 shows that the LGS aberrations for Keck I are circularly symmetric at the center of the pupil, but square symmetric at the edges of the pupil. The circular symmetry arises from the central projection of the laser, and the square symmetry from the square field stop (square extent of the pixels). As shown in Table 1, the only non-zero coefficients of the first 30 Zernike polynomials for Keck I correspond to Zernike polynomials Z_{11} and Z_{22} (circularly symmetric), and Z_{14} and Z_{26} (square symmetric). These four polynomials are shown in Fig. 13. If the field stop were circular instead of square, the coefficients of the square symmetric (Z_{14} and Z_{26}) polynomials are near zero, showing these aberrations arise due to the square field stop. However, the circular field stop leads to a higher spherical aberration coefficient (49 nm), such that the total aberration is greater with a circular stop than a square stop.

#79346 - $15.00 USD Received 24 Jan 2007; revised 19 Mar 2007; accepted 29 Mar 2007; published 3 Apr 2007

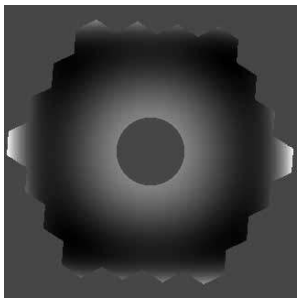

Fig. 12. The simulated total low order LGS aberration for the centrally projected Keck I at 0° pupil angle and at zenith.

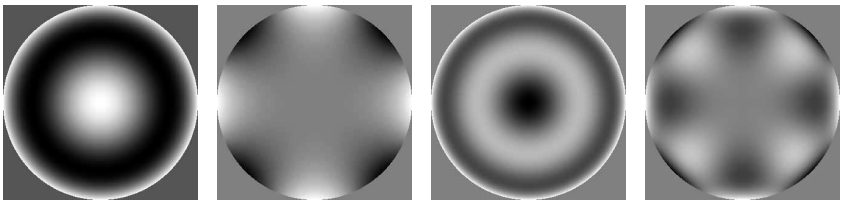

(a) (b) (c) (d)

Fig. 13. The Zernike polynomials corresponding to non-zero LGS aberration coefficients for a centrally projected laser: (a) Z_{11}, (b) Z_{14}, (c) Z_{22}, and (d) Z_{26}.

Table 1. LGS aberrations in Zernike polynomials for the Palomar, Keck I and TMT LGS AO systems for the sum of two Gaussians sodium profile.

Zernike polynomial	Coefficient of LGS aberration (nm)		
	Palomar	Keck I	TMT
Z_{11}	5	34	834
Z_{14}	0	25	338
Z_{22}	0	4	42
Z_{26}	0	7	158
Total	5	43	915

The total modeled LGS aberration of 43 nm for Keck I is significantly less than the modeled aberration for Keck II of 400 nm. This is due to the central projection of Keck I compared to the side projection of Keck II.

5.3. TMT

The Thirty Meter Telescope (TMT) [17] will have a 30 meter diameter primary and will project the laser from the optical axis. In order to overcome the cone effect, TMT intends to use an asterism of six LGSs: one on-axis, and the other five equally spaced on a ring of radius $35''$ [9]. Because the LGSs are so closely spaced (the difference in zenith angle between any two LGS is $<<$ 1 deg), each LGS will experience approximately the same LGS aberrations, and so we consider here the on-axis LGS only. The proposed LGS WFSs are Shack-Hartmann WFS of the order 60x60 subapertures. TMT will employ the radial format CCD [18], with 16×4 pixels per subaperture of dimension $0.5''$. Here we assume a detector of 16×16 pixels of $0.5''$ to bound the problem. We also assume a square field stop of dimensions $8.0''\times8.0''$, center-of-

#79346 - $15.00 USD Received 24 Jan 2007; revised 19 Mar 2007; accepted 29 Mar 2007; published 3 Apr 2007

Table 2. LGS aberrations in Zernike polynomials for TMT for different sodium profiles.

Zernike polynomial	Coefficient of LGS aberration (nm)		
	Gaussian profile	Sum of 2 Gaussians	Median profile
Z_{11}	260	834	-163
Z_{14}	100	338	-50
Z_{22}	-8	42	9
Z_{26}	29	158	-23
Total	281	915	173

mass centroiding, and that all the subapertures within the extent of the primary mirror are active at any one time. The modeled LGS aberrations for TMT under these assumptions for the three different sodium profiles are shown in Table 2.

As for the centrally projected Keck I system, spherical aberration is the largest coefficient for TMT, followed by Z_{26}, Z_{14} and Z_{22}. These four Zernike coefficients are significantly larger for TMT than for Keck I which is due to the much larger telescope diameter for TMT, meaning that the LGS viewed by the subapertures furthest from the center are more elongated.

NFIRAOS has a stringent total wavefront error constraint of 133 nm rms [8]. Given that the LGS aberrations for all three sodium profiles in Table 2 exceed this requirement, it is imperative to correct for these aberrations. For NFIRAOS, the proposed design includes measuring with the TT NGS WFS the focus variations arising from the height of the sodium layer changing [8]. To meet this error requirement, it may be necessary to measure these four higher order terms (Z_{11}, Z_{14}, Z_{22} and Z_{26}) with the fast wavefront sensor.

6. Conclusions

In this paper, we have modeled the LGS aberrations observed at the W.M. Keck Observatory, and have used this model to characterize the parameter space that affects the LGS aberrations, and also to predict the LGS aberrations of future LGS AO systems. In particular, we note that the LGS aberrations are a strong function of the asymmetry of the sodium structure, and this explains the significant difference in magnitude of the LGS aberrations between nights. The LGS aberrations can be significantly reduced by central projection of the laser, and by increasing the FOV of the WFS detector. For TMT, a 30 m telescope with a centrally projected laser, the expected LGS aberrations, if uncorrected, are several times the total wavefront error budget. Careful thought on the best method to correct for these aberrations is required, including measuring the significant high order terms (Z_{11}, Z_{14}, Z_{22} and Z_{26}) concurrently with the focus measurement from the NGS required to detect altitude variations in the sodium layer.

Acknowledgments

The data presented herein were obtained at the W. M. Keck Observatory, which is operated as a scientific partnership among the California Institute of Technology, the University of California, and the National Aeronautics and Space Administration. The Observatory was made possible by the generous financial support of the W. M. Keck Foundation. The authors wish to recognize and acknowledge the significant cultural role and reverence that the summit of Mauna Kea has always had within the Hawaiian community. We are most fortunate to have the opportunity to conduct observations from this mountain. This work has been supported by the National Science Foundation Science and Technology Center for Adaptive Optics, managed by the University of California at Santa Cruz under cooperative agreement No. AST - 9876783.

#79346 - $15.00 USD Received 24 Jan 2007; revised 19 Mar 2007; accepted 29 Mar 2007; published 3 Apr 2007